JOURNAL OF GEOPHYSICAL RESEARCH: SPACE PHYSICS, VOL. 118, 45–57, doi:10.1029/2012JA018064, 2013

Solar wind forcing at Mercury: WSA-ENLIL model results

Daniel N. Baker,[1] Gangkai Poh,[1,2] Dusan Odstrcil,[3,4] C. Nick Arge,[5] Mehdi Benna,[6] Catherine L. Johnson,[7,8] Haje Korth,[9] Daniel J. Gershman,[2] George C. Ho,[9] William E. McClintock,[1] Timothy A. Cassidy,[1] Aimee Merkel,[1] Jim M. Raines,[2] David Schriver,[10] James A. Slavin,[2] Sean C. Solomon,[11,12] Pavel M. Trávníček,[13] Reka M. Winslow,[7] and Thomas H. Zurbuchen[2]

Received 27 June 2012; revised 5 November 2012; accepted 2 December 2012; published 31 January 2013.

[1] Analysis and interpretation of observations from the MESSENGER spacecraft in orbit about Mercury require knowledge of solar wind "forcing" parameters. We have utilized the Wang-Sheeley-Arge (WSA)-ENLIL solar wind modeling tool in order to calculate the values of interplanetary magnetic field (IMF) strength (B), solar wind velocity ($\mathbf{V}$) and density (n), ram pressure ($\sim nV^2$), cross-magnetosphere electric field ($\mathbf{V} \times \mathbf{B}$), Alfvén Mach number ($M_A$), and other derived quantities of relevance for solar wind-magnetosphere interactions. We have compared upstream MESSENGER IMF and solar wind measurements to see how well the ENLIL model results compare. Such parameters as solar wind dynamic pressure are key for determining the Mercury magnetopause standoff distance, for example. We also use the relatively high-time-resolution **B**-field data from MESSENGER to estimate the strength of the product of the solar wind speed and southward IMF strength (B_s) at Mercury. This product VB_s is the electric field that drives many magnetospheric dynamical processes and can be compared with the occurrence of energetic particle bursts within the Mercury magnetosphere. This quantity also serves as input to the global magnetohydrodynamic and kinetic magnetosphere models that are being used to explore magnetospheric and exospheric processes at Mercury. Moreover, this modeling can help assess near-real-time magnetospheric behavior for MESSENGER or other mission analysis and/or ground-based observational campaigns. We demonstrate that this solar wind forcing tool is a crucial step toward bringing heliospheric science expertise to bear on planetary exploration programs.

Citation: Baker, D. N., et al. (2013), Solar wind forcing at Mercury: WSA-ENLIL model results, *J. Geophys. Res. Space Physics*, *118*, 45–57, doi:10.1029/2012JA018064.

1. Introduction

[2] A combination of empirical and numerical modeling methods has produced remarkable strides in the comprehensive understanding of solar wind conditions throughout the inner heliosphere [*Arge et al.*, 2004; *Odstrcil et al.*, 2004a]. This work was, at least initially, motivated by the goal of providing improved forecasts of ambient solar wind conditions at Earth's location for so-called "space weather" purposes. The modeling methods, which will be described and utilized in this paper, rely on remote observations of the Sun from Earth-based instruments combined with empirical and physics-based numerical modeling tools. The operational use of such modeling has demonstrated continuously improving capabilities for space weather prediction for both quiet and disturbed solar conditions.

[1]Laboratory for Atmospheric and Space Physics, University of Colorado, Boulder, Colorado, USA.
[2]Department of Atmospheric, Oceanic and Space Sciences, University of Michigan, Ann Arbor, Michigan, USA.
[3]Computational and Data Sciences, George Mason University, Fairfax, Virginia, USA.
[4]Heliophysics Science Division, NASA Goddard Space Flight Center, Greenbelt, Maryland, USA.
[5]Air Force Research Laboratory, Kirtland Air Force Base, New Mexico, USA.

Corresponding author: D. N. Baker, Laboratory for Atmospheric and Space Physics, University of Colorado, Boulder, CO 80303, USA. (Daniel.Baker@LASP.colorado.edu)

2169-9380/13/2012JA018064

[6]Solar System Exploration Division, NASA Goddard Space Flight Center, Greenbelt, Maryland, USA.
[7]Department of Earth, Ocean, and Atmospheric Sciences, University of British Columbia, Vancouver, British Columbia, Canada.
[8]Planetary Science Institute, Tucson, Arizona, USA.
[9]The Johns Hopkins University Applied Physics Laboratory, Laurel, Maryland, USA.
[10]Institute of Geophysics and Planetary Physics and Department of Physics and Astronomy, University of California, Los Angeles, California, USA.
[11]Department of Terrestrial Magnetism, Carnegie Institution of Washington, Washington, D.C., USA.
[12]Lamont-Doherty Earth Observatory, Columbia University, Palisades, New York, USA.
[13]Space Sciences Laboratory, University of California, Berkeley, California, USA.

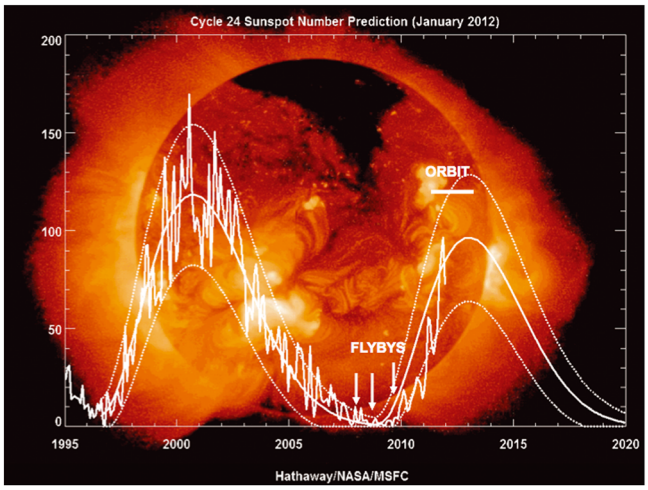

Figure 1. Average sunspot number versus time from 1995 to early 2012 [courtesy of D. Hathaway, NASA Marshall Space Flight Center]. The times of the MESSENGER flybys of Mercury are indicated by vertical arrows, and the duration of MESSENGER's primary and first extended orbital mission is shown by the horizontal bar.

[3] In previous work [*Baker et al*., 2009, 2011], we have shown the solar wind conditions as modeled—and as observed—for the three Mercury flybys by the MErcury Surface, Space ENvironment, GEochemistry, and Ranging (MESSENGER) spacecraft in 2008–2009. In that work, we noted the limitations of having only a single-point measurement at the MESSENGER location in the inner heliosphere. A much broader and more comprehensive context can be set for in situ spacecraft observations if there is a global map of inner heliospheric solar wind plasma and magnetic field conditions. From the state-of-the-art modeling techniques that we use, it is possible to provide a clearer picture of high-speed solar wind streams, corotating interaction regions, interplanetary magnetic field (IMF) sector boundaries, and heliospheric current sheet properties throughout the inner solar system. The first MESSENGER flyby of Mercury (M1) in January 2008 and the second flyby (M2) in October 2008 were fully successful from the standpoint of MESSENGER data collection, and the third flyby (M3) in September 2009 also provided remarkable new data for the available data interval of that passage [see *Baker et al*., 2011, and references therein].

[4] In this paper, we first summarize our modeling techniques. We then provide detailed new results for the period forward from March 2011 during which MESSENGER has been in orbit around Mercury. In our earlier work, we demonstrated that the available spacecraft data from near 1 AU allowed us to "calibrate" the solar wind and interplanetary magnetic field modeling for consistency and overall validity. We have again used measurements from the Advanced Composition Explorer (ACE) and the Solar TErrestrial RElations Observatory (STEREO) pair of spacecraft in this study to assess the general model validity and utility of the model. We have compared the local model results near Mercury directly with available upstream MESSENGER measurements for the approximately 9 month period of this analysis. Finally, we show here how the model data can be used to order and organize MESSENGER observations of processes and phenomena inside the magnetosphere and exosphere of Mercury.

[5] The MESSENGER measurements have shown that Mercury's internal magnetic field is largely dipolar, aligned with the planetary axis, and of the same polarity as Earth's field [*Anderson et al*., 2008, 2010, 2012; *Alexeev et al*., 2010]. These same observations have shown that Mercury's magnetosphere resembles that of Earth with respect to its structure [*Johnson et al*., 2012], but its response to changes in the upstream solar wind and interplanetary magnetic field is more extreme and occurs on timescales of just ~2–3 min [Slavin *et al*., 2009, 2010; *Siscoe et al*., 1975] rather than ~40–60 min as at Earth [*McPherron et al*., 1973; *Baker et al*., 1996]. Dayside reconnection and tail loading and unloading have been observed at Mercury, but the intensity of the dayside reconnection and the amplitude of the tail magnetic field increases are much larger than what is observed at Earth [*Slavin et al*., 2009, 2010]. Although terrestrial-style substorms and electrodynamic coupling between a conducting ionosphere and a magnetosphere via steady field-aligned currents cannot take place at Mercury, MESSENGER observations of plasmoid ejection, charged particle acceleration, and magnetic dipolarization events in the magnetotail plasma sheet are all indicators of substorm-like activity at Mercury [see *Sundberg et al*., 2012].

[6] MESSENGER's three flybys of Mercury occurred during the most extended and deepest minimum of solar activity in nearly two centuries. Figure 1 shows the monthly sunspot number from 1995 to January 2012. It is clear that the solar forcing conditions during the times of the three MESSENGER flybys were at the very minimum of the approximately 11 year activity cycle. It is also clear that by the beginning of 2011, solar activity (as measured by average sunspot number) had begun to pick up markedly. By March 2011, when MESSENGER entered orbit about Mercury, solar activity had begun to approach the level that had been previously predicted (as shown by the smooth solid curve in Figure 1). Quite obviously, the period following Mercury orbit insertion has been one of much more frequent and powerful solar forcings of the Mercury system than was the case during the three planetary flyby periods.

2. Model Description and Data Sources

[7] As discussed previously by *Baker et al*. [2011], the Wang-Sheeley-Arge (WSA) model involves combined empirical and physics-based forecasts of the global solar wind flow [*Arge and Pizzo*, 2000; *Arge et al*., 2004]. It is used to predict the solar wind speed and IMF strength at Earth (as well as other points in the inner heliosphere) and is an extension of the original *Wang and Sheeley* [1992] model. The model uses ground-based observations of the solar surface magnetic field as input to a magnetostatic potential-field source surface (PFSS) model [*Schatten et al*., 1969] to estimate the current sheet properties between 2.5 and 5 R_S (Figure 2), where R_s is the solar radius. For the work reported here, solar magnetic field maps updated once per day (24 h cadence) were used. Outward flows in the corona were approximated by the imposition of radial field boundary conditions at the source surface and by empirical relationships of expansion factors to initialize solar wind speeds at this point. This surface is a Sun-centered sphere of radius 21.5 R_s.

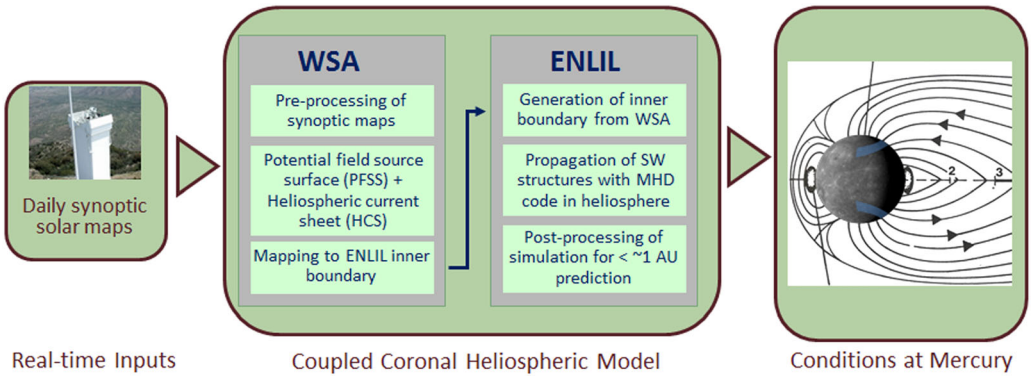

Figure 2. The observational and modeling elements that constitute the Wang-Sheeley-Arge (WSA) and ENLIL tools used in this study.

[8] Photospheric field observations are the basic properties that drive the modeling. They serve as a key input to the coronal and solar wind models. Updated photospheric magnetic maps, incremented regularly with new data, were constructed with magnetograms from the National Solar Observatory's Global Oscillation Network Group (GONG) data set. The line-of-sight field measurements from these data sources were converted to the radial field component [*Arge et al.*, 2004]. The radial magnetic field is the basis of the standard "forecast" version of the models. In this paper, as noted above, data from GONG were updated at a 24 h cadence and had scaled model parameters for the extended study.

[9] Building upon WSA results for the region near the Sun, an ideal magnetohydrodynamic simulation, ENLIL, was subsequently used to model the solar wind flow outward to distances beyond 1 AU [*Odstrcil et al.*, 2004b]. The computational domain was a uniform grid in latitude and longitude occupying the sector of a sphere. The position of the inner boundary was at 0.1 AU ($\approx$21.5 R_s), and the outer boundary was commonly set at 1.7 AU. The meridional and azimuthal ranges spanned 30°–150° in heliospheric colatitude and 0°–360° in longitude, respectively. The inner boundary lies in the supersonic flow region. The outer boundary at 1.7 AU allowed comparison of simulated temporal profiles of solar wind properties at and near the Earth's position with spacecraft measurements by ACE or other space platforms [e.g., *Odstrcil et al.*, 2004a, 2004b].

[10] The combined WSA-ENLIL modeling provides specification of the solar wind flow speed, plasma density, solar wind mean plasma temperature, and magnetic field strength throughout the inner heliosphere. As an example, a color representation of the radial flow speed (V_r) and density (n) of the solar wind plasma in the heliospheric equatorial plane computed for the entire inner heliosphere on 3 May 2011 is shown in Figure 3. The model results in this snapshot demonstrate that a broad solar wind stream region was present near the ecliptic plane during this time. The modeled solar wind speed enhancements (up to speeds of ~600 km/s) at ~1 AU were primarily in the longitude sector encompassing the azimuthal location of the Earth (i.e., −45° to +45° longitude). According to the model, the stream had not yet enveloped the STEREO-A spacecraft at the time of the snapshot but had passed the STEREO-B several days earlier.

[11] The MESSENGER and Mercury were (obviously) collocated at the time shown in Figure 3 and were subjected to essentially the same solar wind flow conditions. From the perspective of Mercury's magnetosphere, there was a modest solar wind speed enhancement expected on the day of this snapshot. The high-speed stream noted above would have further encountered MESSENGER for several days following the time of the image with the highest-speed (600 km/s) stream features expected to rotate over the Mercury location some 1–2 days later.

[12] *Baker et al.* [2009, 2011] emphasized that correct characterization of the solar wind stream properties at the three separated spatial locations (ACE, STEREO-A, and STEREO-B) constitutes an important validation of the model's overall capabilities. The stream arrival times in the model were found to be reasonably similar to the observations at the three widely spaced observing points (data not shown here). Such results confirm that the solar wind pattern in the inner heliosphere is essentially as predicted by the model and as illustrated in Figure 3. Our comparisons with the model output show that WSA-ENLIL normally does a satisfactory job of characterizing the solar wind and IMF data near, ahead, and behind the Earth locations as seen by the ACE and STEREO-A and -B spacecraft comparisons for the 2011 periods modeled in this paper.

[13] For the present study, we used the WSA-ENLIL modeling results in conjunction with measurements from several MESSENGER spacecraft instruments. We placed particular emphasis on direct comparisons with observations by MESSENGER's Magnetometer (MAG) [*Anderson et al.*, 2007] and the Fast Imaging Plasma Spectrometer (FIPS) [*Zurbuchen et al.*, 1998; *Andrews et al.*, 2007] and Energetic Particle Spectrometer (EPS) sensors on the Energetic Particle and Plasma Spectrometer (EPPS) [*Andrews et al.*, 2007].

3. Solar Wind and IMF Data—Model Comparisons

[14] A broad synoptic view of the WSA-ENLIL model output covering the period from ~1 March 2011 to December 2011 is shown in Figure 4. The panels show (from the first panel) the computed IMF field strength (B), solar wind density (n), solar wind speed (V), and mean solar wind temperature (T). The fifth and sixth panels of Figure 4 show the useful composite parameters Alfvén Mach number, M_A, and solar wind dynamic pressure, P_{dyn} ($=\rho V^2$, where $\rho = nm$ and m is the proton mass). Together, these computed model outputs provide the best available estimate of the ambient forcing conditions imposed by the solar wind at Mercury's location.

[15] Some obvious features reveal themselves in the model data. In the first panel (B) and also in the sixth panel

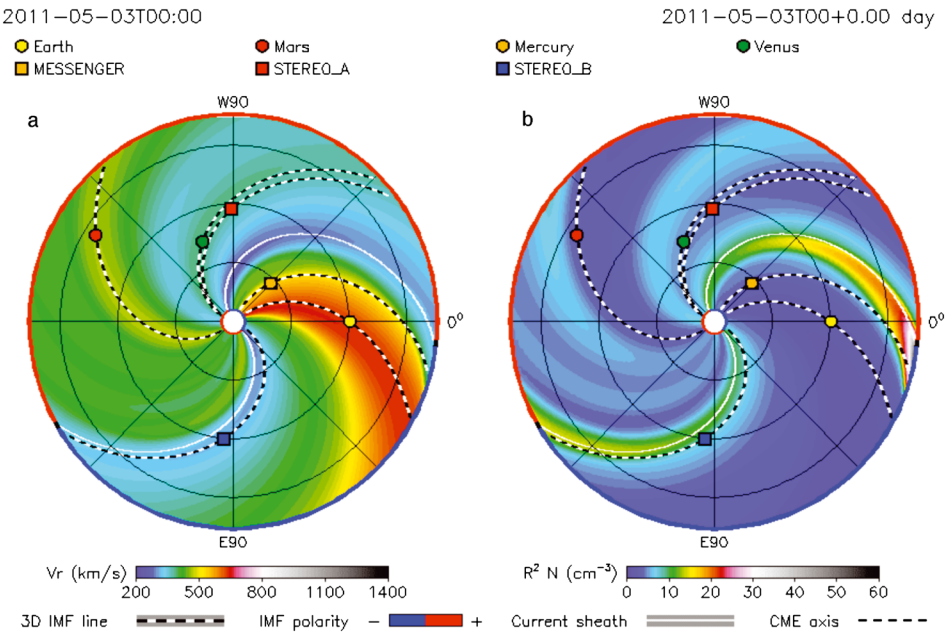

Figure 3. (a) Modeled radial solar wind speed, viewed from the north ecliptic pole, obtained from the WSA-ENLIL model at an exemplary time when MESSENGER was in orbit around Mercury (3 May 2011). The scale for V_r is given by the color bar. The locations of Earth, STEREO-A, STEREO-B, Venus, Mercury, Mars, and the MESSENGER spacecraft are indicated by small colored symbols. The inner domain of the model (where WSA is utilized) is denoted by the white central circle. The computational domain of the ENLIL simulation is shown by the colored area. The red-blue color coding along the edge of the outer boundary of computation shows the polarity of the IMF: red indicates IMF positive, or pointing away from the Sun, and blue indicates negative polarity with the IMF pointing toward the Sun. The white curves mark estimated IMF polarity sector boundaries near the equatorial plane. (b) WSA-ENLIL model results for density of the solar wind (normalized to 1 AU) for the period shown in Figure 3a.

(P_{dyn}), we see a clear periodic pattern of higher and then lower computed values. The period of this large-scale oscillation is about 90 days. This variation is quite evidently associated with the 88 day orbital motion of Mercury around the Sun. Because of its relatively high orbital eccentricity, Mercury's heliocentric distance d varies from about 0.3 AU to more than 0.45 AU during one Mercury year. Past experience has shown that solar wind density and IMF strength decrease systematically with geocentric distance. As such, the planet (and consequently MESSENGER in orbit around the planet) will experience large swings in the average solar wind density (falling off as d^{-3}) and magnetic field strength (falling off as $\sim d^{-2}$). It is interesting that the n, T, and V parameters calculated from WSA-ENLIL show considerable temporal structure due to the solar wind stream properties that are captured by the modeling. However, it is B and P_{dyn} that show the heliocentric-distance effect the most smoothly and clearly.

[16] The model values for V and T closely correlate with one another throughout the period of analysis (Figure 4). On the other hand, the values of density tend to anticorrelate with V (and T) in many instances. Also note that the computed Alfvén Mach numbers, generally ranging in value between 5 and 10, are broadly anticorrelated with the dynamic pressure values. This anticorrelation follows naturally from the definition of M_A and the strong 88 day variations seen in B as portrayed in Figure 4. The shorter-period (10–20 day) variations in the V, T, and n parameters are due to solar wind stream structures [see *Baker et al.*, 2009, 2011], which WSA-ENLIL models quite effectively.

[17] It is important to note that all of the calculated solar wind and IMF values shown in Figure 4 are estimates of ambient solar wind properties [e.g., *Odstrcil and Pizzo*, 1999; *Odstrcil et al.*, 2004b]. For this purpose, no attempt has been made in the computations shown in the figure to include transient disturbances such as coronal mass ejections (CMEs) or related shock waves. Below we describe efforts to utilize the "cone model" [*Zhao et al.*, 2002; *Xie et al.*, 2004] extension to WSA-ENLIL to capture CMEs and other solar energetic particle events superimposed upon the ambient solar wind flow.

[18] A comparison of MESSENGER magnetic field measurements with the WSA-ENLIL model results is shown in Figure 5 as a function of day of year (DOY) during 2011. The MESSENGER data have been carefully screened [*Korth et al.*, 2011; *Winslow et al.*, 2012] to assure that MAG results only upstream of the Mercury bow shock are included in the plot.

[19] Overall, Figure 5 shows that the typical MAG values at any given time are in good agreement with the ENLIL values. Obviously, there is considerable variance in the MAG values, but the ENLIL curve follows the longer-term trends in the MESSENGER data quite well. Careful inspection shows that early in the comparison interval (DOY $\leq$ 200), the ENLIL values ride consistently lower than the MAG results. After about DOY 240 or so, the ENLIL model

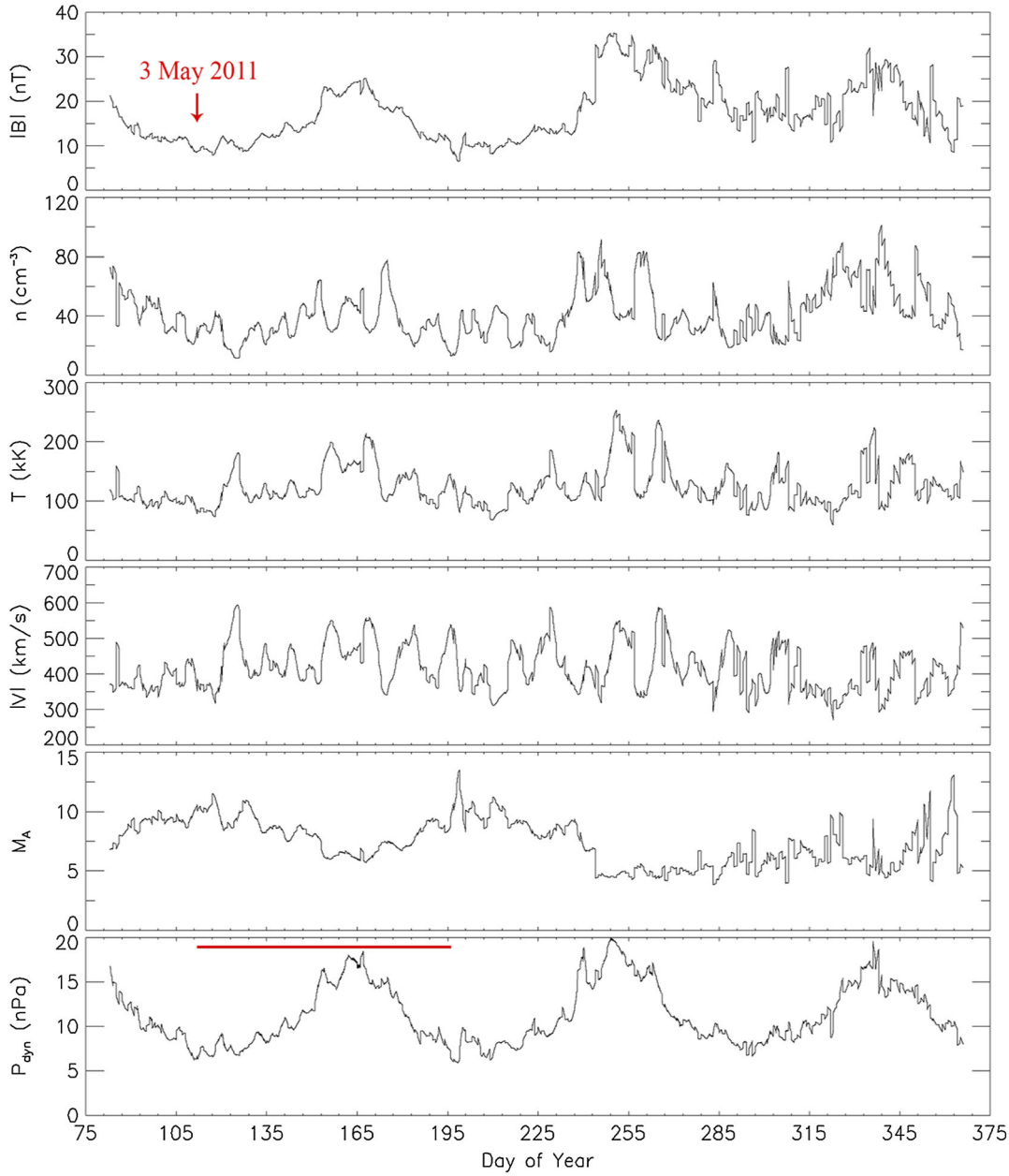

Figure 4. The WSA-ENLIL model results for the period March 2011 through December 2011. Computed values of IMF B, n, T, V, M_A, and P_{dyn} are shown from the first to the sixth panels, respectively. The red bar in the sixth panel shows the duration of the 88 day Mercury orbit around the Sun. The time of the snapshot shown in Figure 3 is indicated by the arrow in the first panel.

values tend to be higher than the typical MAG values. The reason for this systematic change in relative values of model and data values is still being examined, but it may be related to increased CME activity.

[20] Perhaps one of the most striking aspects of Figure 5 is the abundance of spikes in the MESSENGER data that stick far above the baseline of MAG values (and above the ENLIL model curve). These spikes are due to CME passages (with stronger magnetic fields in and draped around the CMEs) and other transient solar wind features that are not included in the ambient WSA-ENLIL modeling. As can be seen in the figure, these transient events can last for several days, and the magnetic field strengths during such episodes can often exceed $B_{IMF} = 40$ nT. The largest events (as in June 2011 and November 2011) can have $B_{IMF} > 80$ nT on average. These events represent very strong forcings of the Mercury system.

[21] In analogy with Figure 5, we show comparisons of WSA-ENLIL results with FIPS measurements of solar wind speed in Figure 6a and solar wind temperature in Figure 6b. As described previously by *Baker et al.* [2011], because of the physical placement of the FIPS sensor on the MESSENGER spacecraft as well as spacecraft pointing constraints, it is not possible to obtain continuous and complete measurements of the plasma distribution functions. However, new retrieval methods [*Gershman et al.*, 2012] have greatly increased the

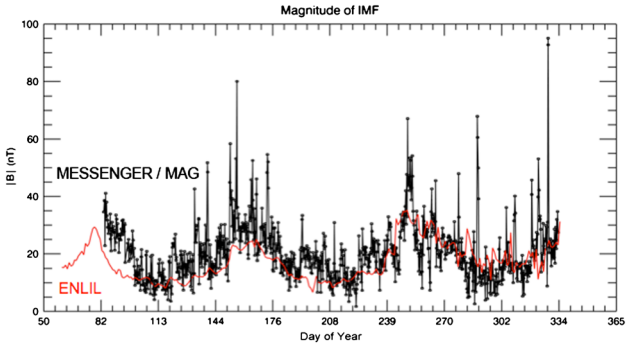

Figure 5. Comparison of MESSENGER interplanetary magnetic field observations (black dots) with ENLIL model results (red curve) from March 2011 to November 2011 (as discussed in the text).

frequency and accuracy of FIPS solar wind parameter determinations. The data points in Figures 6a and 6b show the available measured FIPS results throughout our analysis interval.

[22] From inspection of Figure 6a, we conclude that the modeled solar wind speeds generally fit the trends of the MESSENGER data. It appears that the agreement is better (for the most part) later in the comparison interval. Given the challenges of retrieving the true measured solar wind speeds, we argue that the ambient WSA-ENLIL values of V are probably the best forcing parameters we can use. We again note, however, that the ENLIL values in Figure 6a do not replicate the high-speed solar wind flows that would accompany CMEs and interplanetary shock waves.

[23] Directly analogous remarks can be made about the WSA-ENLIL comparisons to FIPS solar wind temperature measurements in Figure 6b. In general, the data-model comparisons are reasonably good, and the trends are similar. Here again, we would suggest that for several of the cases in which FIPS measured temperatures were much higher than the modeled values, there could have been transient solar wind disturbances.

[24] Because of the powerful trends seen in various solar wind and IMF quantities imparted by Mercury's large excursions in heliocentric distance, we have modeled, and endeavored to remove, orbital trends from the ENLIL-generated parameters. Figure 7 shows in the first panel the ENLIL-computed dynamic solar wind pressure (see Figure 4 above). Overplotted on the model output is a simple trend curve that depends solely on the heliocentric distance of Mercury. As can be readily seen, the smooth curve follows the general pressure excursions closely. This orbital effect evidently accounts for the largest-scale and lowest-frequency excursions of P_{dyn}.

[25] In the second panel of Figure 7, we show δP_{dyn}, the difference between the ENLIL-generated values and the smooth trend curve in the first panel. This curve shows the "residual" dynamic pressure variations computed within the model. Similarly, in the third panel of Figure 7, we show the residual values of modeled solar wind density (δn), and in the fourth panel we show the residual values of the IMF magnitude (δB). Perhaps the most surprising feature in all of the panels is the large systematic departure of δB from the "baseline" values for the period from DOY ~240 through DOY ~320. This offset is still being evaluated in our modeling efforts.

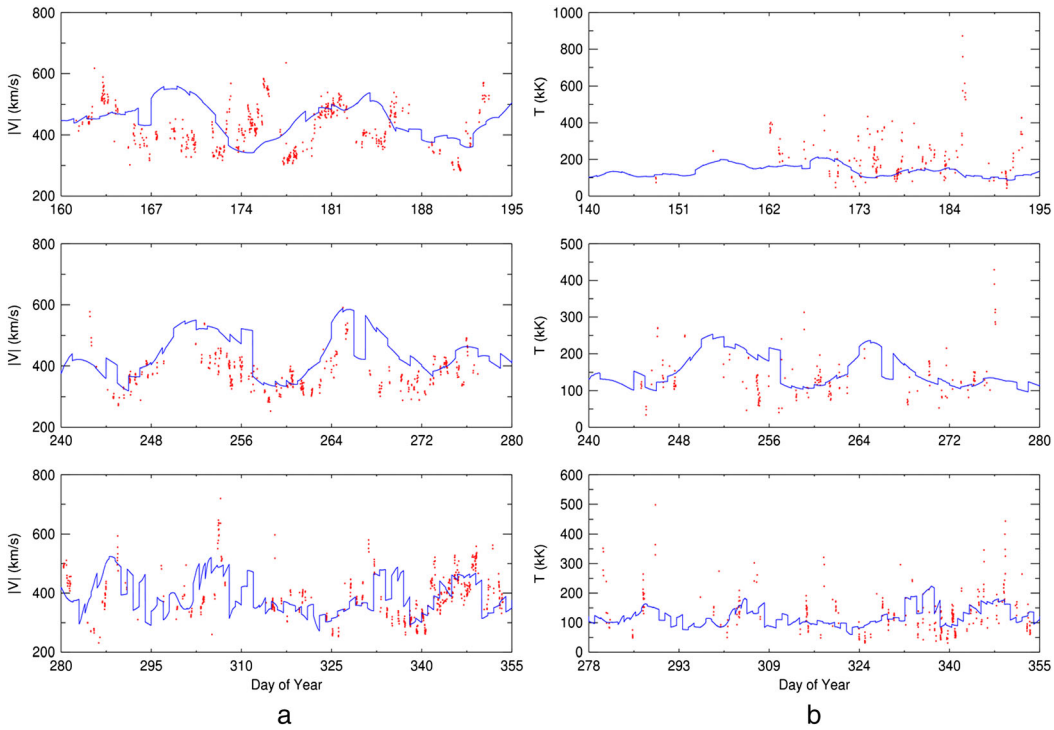

Figure 6. (a) Comparison of MESSENGER solar wind plasma flow speed observations (red dots) and ENLIL model results (blue curves) as discussed in the text. (b) Comparison of solar wind temperature from the ENLIL model (blue curves) and MESSENGER observations (red dots).

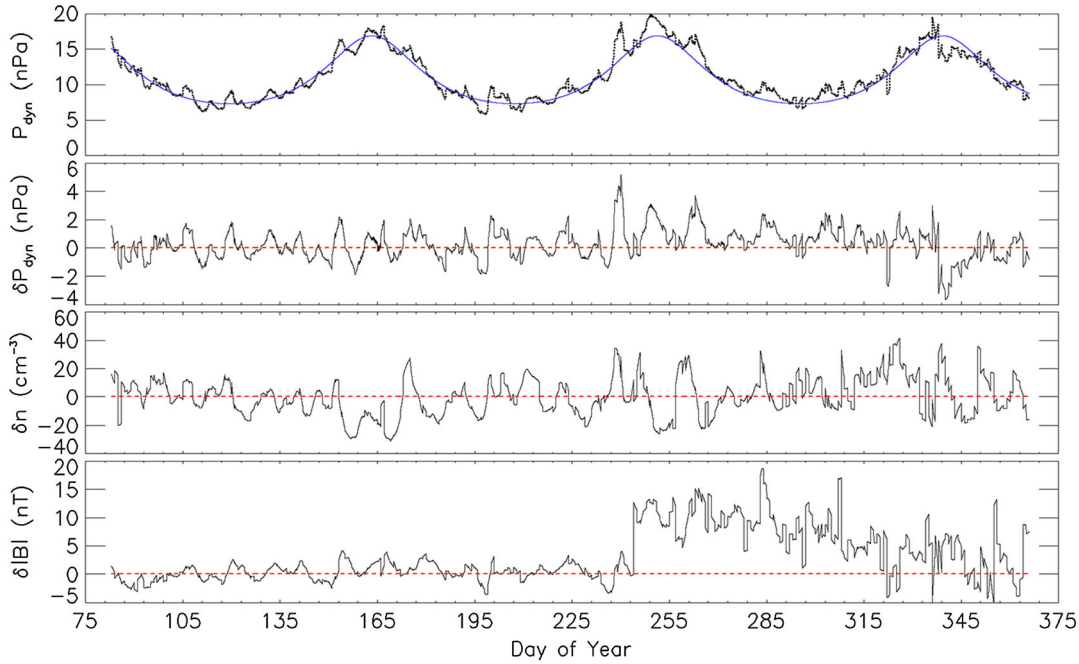

Figure 7. Similar to Figure 4, but showing removal of orbital trend effects. The first panel shows P_{dyn} (see Figure 4) with a smooth trend curve superimposed. The second to fourth panels show, respectively, the WSA-ENLIL modeled dynamic pressure, density, and average magnetic field strength with the corresponding smooth trends removed.

[26] As noted above, a full treatment of solar wind modeling would require inclusion of CMEs and other transient interplanetary features. The much more active Sun during 2011–2012 (see Figure 1) compared with 2008–2010 means that many interplanetary transients are now occurring each month. The community [see *Pizzo et al.*, 2011] has been using the cone model extension to WSA-ENLIL to capture CME behavior. Figure 8 shows a striking example of this capability for a period of highly disturbed solar wind in late November 2011. This figure is the cone-model equivalent of the ambient model polar projection shown in Figure 3.

[27] In Figure 8, a localized, dense, crescent-shaped feature may be seen to have moved out through the heliosphere. The feature was located primarily in the 0°–90°W

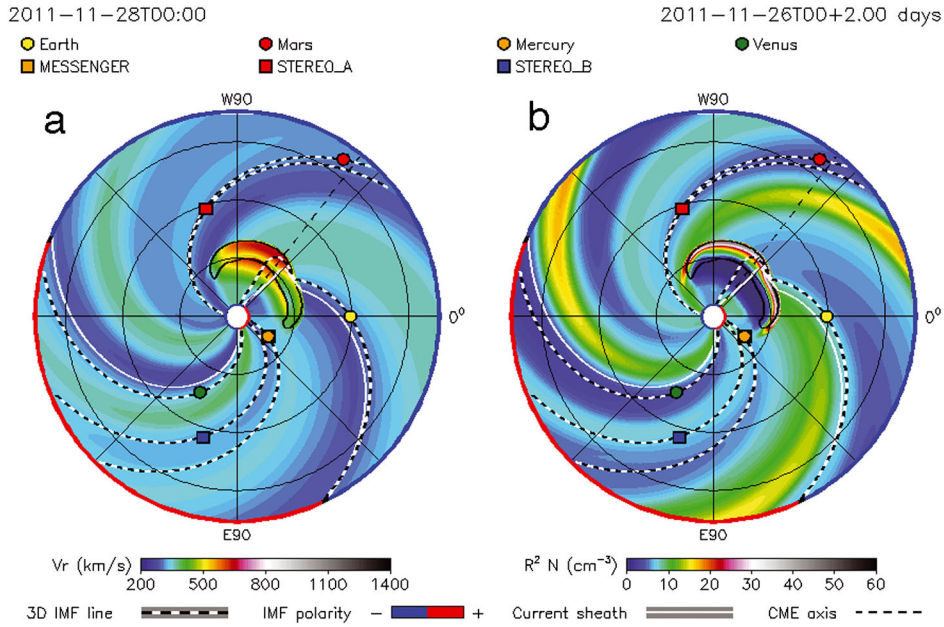

Figure 8. Model similar to that in Figure 3 but utilizing the "cone model" version of WSA-ENLIL with a propagating CME (outlined in black) as seen on 28 November 2011. (a) Solar wind speed profile. (b) Density map for the same period as Figure 8a.

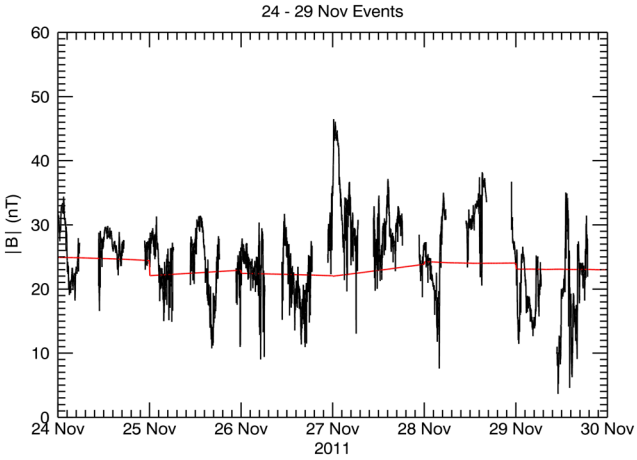

Figure 9. Detailed values of interplanetary magnetic field (MAG) data from MESSENGER for the period 26–29 November 2011 showing the strong transient event (CME) that impacted the Mercury system early on 27 November 2011.

longitudinal sector of the ecliptic plane. In the full WSA-ENLIL cone simulation, the CME in the model started at 0700 UTC on 26 November 2011, and it swept past Mercury (and MESSENGER) early on 27 November. The CME impacted Earth rather squarely on 28 November and also hit the STEREO-A spacecraft on 28 November as well. This CME was one of the stronger events from the Sun seen during the period of resurgent solar activity in late 2011.

[28] Details of the MESSENGER measurements of magnetic field and ENLIL modeling for this active November 2011 period are shown in Figure 9. The data show that the IMF B values typically ranged from ~15 to ~30 nT. The ENLIL modeling showed an estimated value of B ranging from ~25 nT at the beginning of the period down to a value of ~22 nT at the end of the interval. Thus, the typical value of B_{IMF} measured by MAG on MESSENGER agreed reasonably well with the ENLIL model results. A strong enhancement of B_{IMF} showing a rapid rise (and slower decline) commenced right at the beginning of 27 November. The forecast version of WSA-ENLIL (with the cone extension) predicted that a strong CME would reach MESSENGER at ~0550 UTC on 27 November. Thus, the arrival time predicted by the model was late by some 5–6 h. Otherwise the model fit well the actual observations.

4. Magnetospheric and Exospheric Effectiveness of Solar Wind Forcing

[29] The results presented in the previous section suggest that the ENLIL model outputs are a reasonably accurate portrayal of the solar wind and IMF conditions that affected Mercury over the period from March 2011 onward. Given the challenges to obtaining continuous, accurate measurements of solar wind properties near Mercury [see *Gershman et al.*, 2012], as argued above, WSA-ENLIL model results probably give us the best available solar wind "indices" for studying the magnetospheric and exospheric properties of Mercury. In principle, the ENLIL model results can provide continuous solar wind and IMF parameter estimation. The in situ measurements of such parameters by MESSENGER instruments, of course, can be made only when the spacecraft is outside of the Mercury magnetosphere and upstream of Mercury'a bow shock.

[30] Several of the solar wind and IMF parameters that we might assume a priori would drive Mercury's magnetospheric properties are shown in Figure 4. From experience at Earth, we know that bow shock and magnetopause positions depend strongly on solar wind dynamic pressure, for example [*Shue et al.*, 1997]. Similarly, we know from Earth experience that magnetospheric dynamics and substorms depend strongly on the interplanetary electric field $\mathbf{E}_{IMF}$ [e.g., *Baker et al.*, 1996]. For this latter source of forcing, we know that $\mathbf{E}_{IMF} = \mathbf{V}_{SW} \times \mathbf{B}_{IMF}$. As described in section 3, we believe the value of $\mathbf{V}$ from WSA-ENLIL is a broadly reliable estimator of $\mathbf{V}_{SW}$. A recognized limitation of the ENLIL modeling, however, is that we cannot specify with any great certainty or accuracy the north-south component of the IMF [see *Baker et al.*, 2009, 2011].

[31] Because of these limitations, we have adopted a "hybrid" approach for some purposes. In other words, we have used the WSA-ENLIL model outputs for all solar wind plasma properties (e.g., V, n, T), and we have used the most current available IMF parameters from in situ upstream measurements by the MAG instrument on MESSENGER.

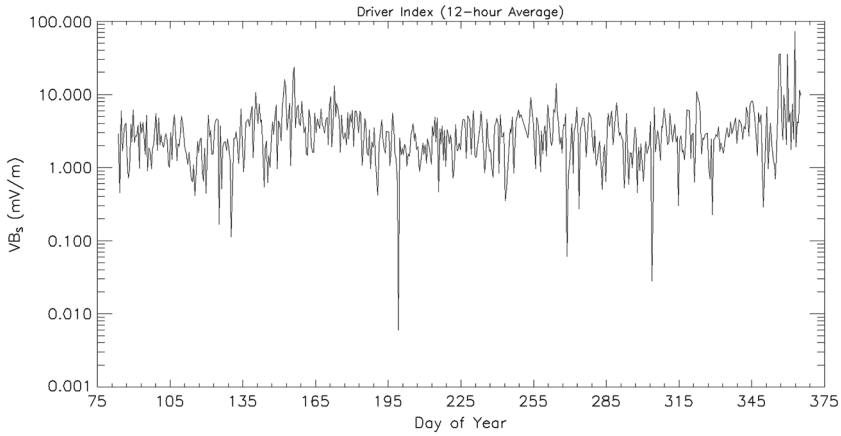

Figure 10. The computed value of VB_s using the ENLIL values of solar wind speed (V) and the MESSENGER values of B_s from DOY ~80 to the end of November 2011.

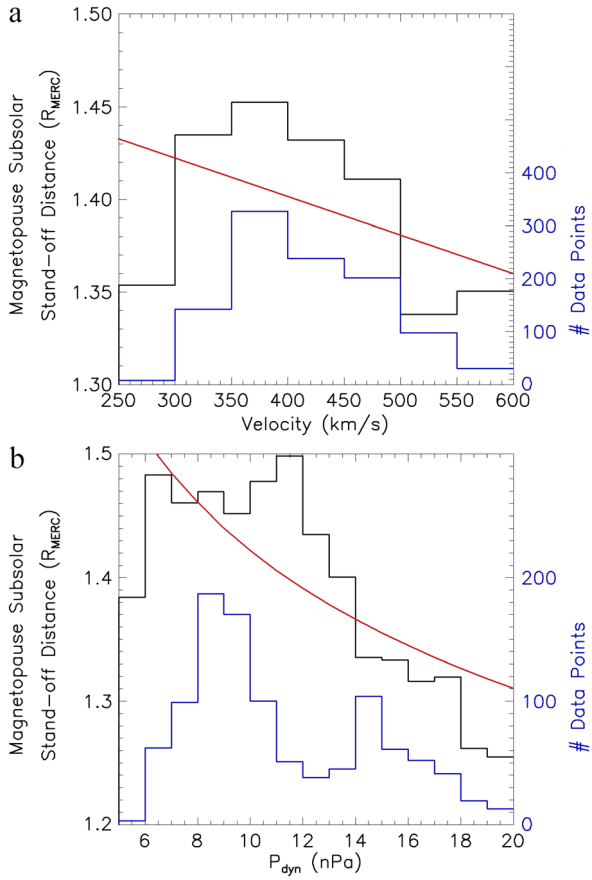

Figure 11. (a) Relation between mean magnetopause standoff distance (in units of Mercury radii, R_M) and solar wind velocity (computed by ENLIL). The red line shows the linear least squares fit of the mean R_{ss} values versus V. The blue histogram (axis to the right) shows the number of magnetopause location values for each solar wind speed interval in the black histograms. (b) Relation between mean magnetopause standoff distance and solar wind dynamic pressure (P_{dyn}) computed by ENLIL. The red curve shows the expected $P_{dyn}^{-1/6}$ dependence of R_{ss} (see text).

Of course, such IMF measurements were not available when the spacecraft was inside the magnetospheric system of Mercury, but for extended portions of each 12 h orbit during MESSENGER's primary orbital mission, there were IMF observations. In particular, actual values of B_s can be specified. The hybrid index, V (ENLIL) B_s (MESSENGER) = VB_s then gives us a crucial estimate of the rectified solar wind electric field, $\mathbf{E}_{IMF}$.

[32] The hybrid forcing index VB_s computed for the period March 2011 to November 2011 is shown in Figure 10. In keeping with the above prescription, we show VB_s as a 12 h average value, and we have used whatever interplanetary B_s values were available in that averaging interval from the MESSENGER MAG data set. The figure shows broad time intervals when VB_s was relatively high in value and shows similarly broad periods when the average VB_s values were low, e.g., 1–2 mV/m. Overall, we would expect the Mercury system to have been subjected to a wide range of solar wind forcing conditions extending over at least two orders of magnitude (i.e., from $VB_s \sim 0.1$ to ~30 mV/m).

[33] How can we utilize the solar wind forcing quantities defined here? Figure 11 provides a specific illustration. In Figures 11a and 11b, we have used the magnetopause subsolar standoff distance (R_{ss}) estimated by R.M. Winslow et al. (Mercury's magnetopause and bow shock from MESSENGER Magnetometer observations, submitted to *Journal of Geophysical Research*, 2012). Figure 11a shows R_{ss} values (in units of Mercury radii, R_M) versus ENLIL solar wind velocity (V). Figure 11b shows R_{ss} values versus P_{dyn}. The

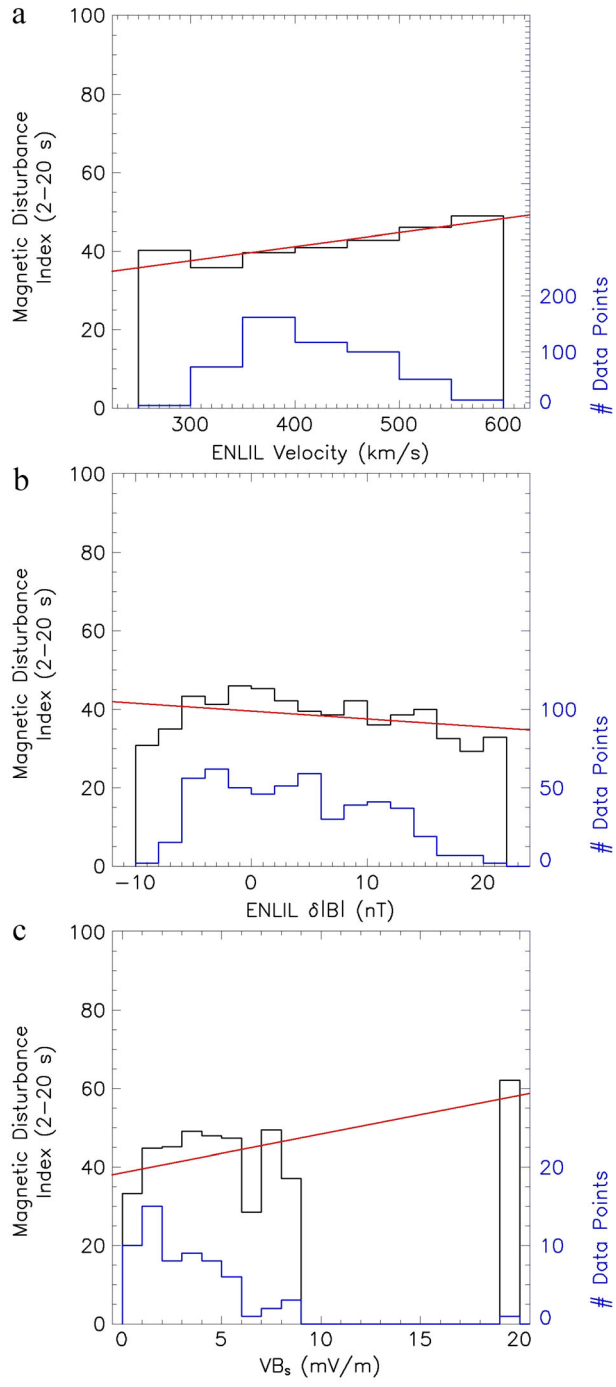

Figure 12. (a) Mean values of magnetic disturbance index (MDI) versus ENLIL-computed solar wind speed. (b) Mean MDI values versus ENLIL δB. (c) Mean MDI values versus hybrid VB_s (as shown in Figure 10).

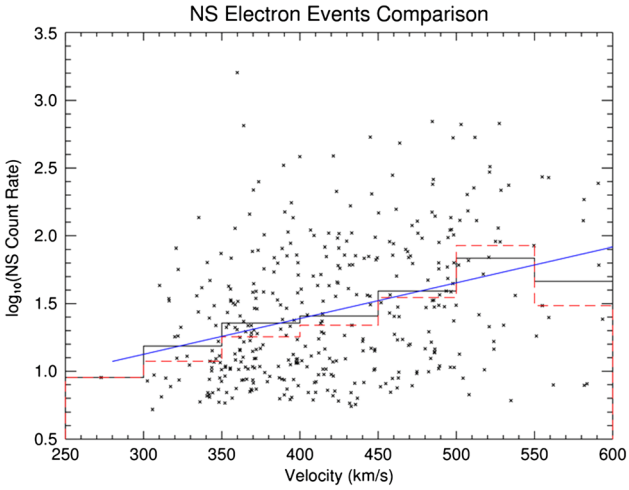

Figure 13. Electron burst event ($E \geq 20$ keV) magnitudes determined from MESSENGER NS count rates versus solar wind speed V (determined from ENLIL). The black histogram is the mean value of the NS counting rates for each V interval. The red dashed histogram is the median value for each corresponding V interval. The blue line is the least squares fit through the individual points.

higher-time-resolution determinations of R_{ss} are quite scattered (*Winslow et al.*, submitted manuscript, 2012), with many hundreds of values acquired from the MESSENGER passages, so we show comparisons with histograms of mean values. In Figures 11a and 11b, we indicate in blue the number of samples that were utilized to derive the values (black histogram). As is clear from the plots, the model solar wind parameters order and organize the mean observed standoff distances fairly well. In Figure 11a, the least squares line fit through the histogram midpoints has a linear correlation coefficient of $r = -0.440$. In Figure 11b, we show the relationship that would be expected for R_{ss} versus P_{dyn}, namely $R_{ss} \sim P_{dyn}^{-1/6}$. We have looked at other parameters (e.g., n, T, M_A), but V and P_{dyn} show the best correlations with R_{ss} (as might have been anticipated). The higher the solar wind speed or dynamic pressure, the more "compressed" is Mercury's magnetosphere (see *Winslow et al.*, submitted manuscript, 2012).

[34] Another interesting relationship to explore has to do with general levels of magnetic activity within the Mercury magnetosphere. *Anderson et al.* [2012] analyzed MESSENGER magnetic field fluctuations for times when the spacecraft clearly was inside the magnetospheric cavity. Both "high-frequency" wave power (periods in the range

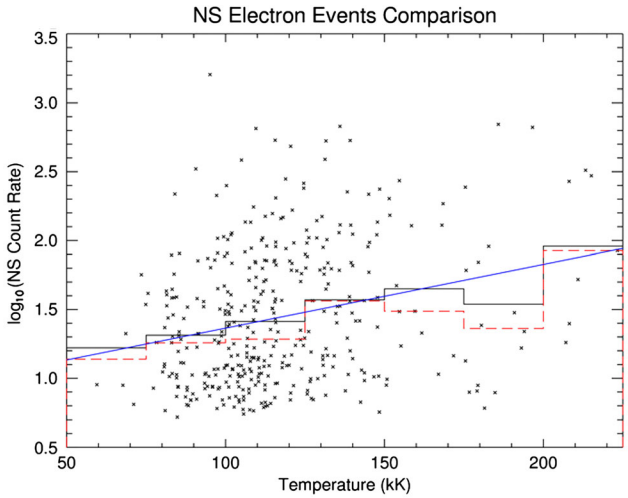

Figure 14. Electron burst event ($E > 20$ keV) magnitudes determined from MESSENGER NS count rates versus solar wind T (derived from ENLIL).

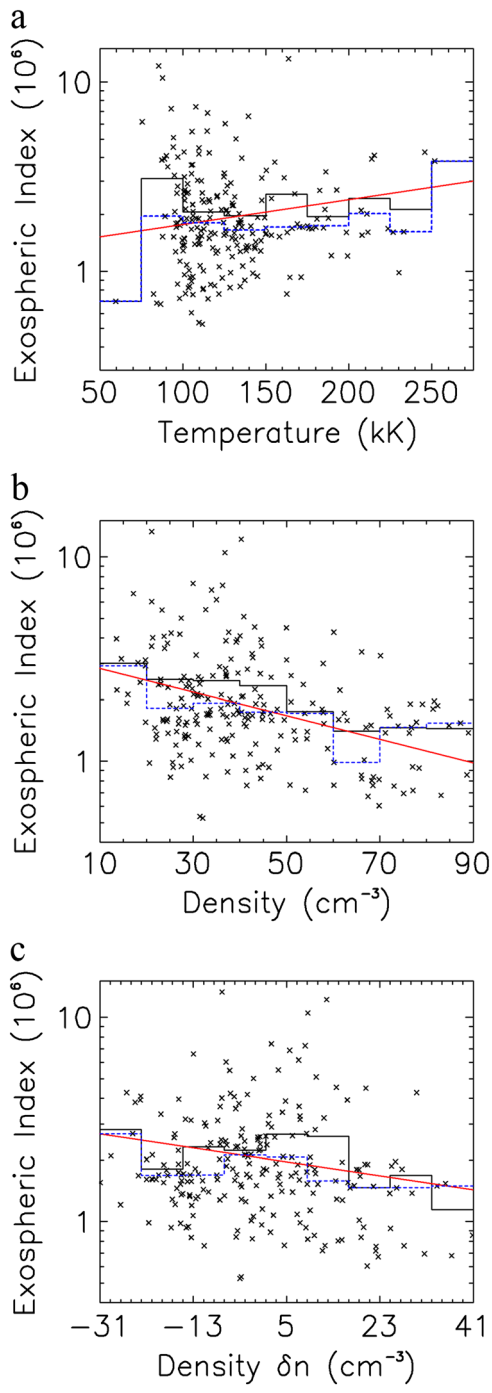

Figure 15. (a) Exospheric sodium index (EI) versus solar wind temperature as described in the text. (b) Exospheric sodium index versus solar wind density as calculated by ENLIL. (c) EI versus detrended ENLIL density (δn).

Table 1. Correlation Coefficients Between Several Properties of Mercury's Atmosphere or Magnetosphere and Modeled Solar Wind Parameters[a]

Solar Wind Index	Velocity (V)	Temperature (T)	Density (n)	VB_s
Magnetopause standoff distance	−0.44 (−0.16)	(−0.28)	(−0.15)	(−)
Magnetic disturbance index	0.88 (0.25)	(−0.05)	(−0.36)	0.56 (0.26)
Neutron Spectrometer count rate	0.94 (0.34)	0.93 (0.25)	(−0.25)	(−)
Sodium exospheric index	(0.03)	0.55 (0.06)	−0.95 (−0.05)	(−)

[a]Values in parentheses are "raw" correlations as discussed in the text whereas nonparenthetical entries are correlations for binned data.

2–20 s) and "low-frequency" wave power (periods of 20–300 s) were assessed. In Figure 12, we show histograms of the mean values of the 2–20 s magnetic disturbance index (MDI) plotted versus several solar wind parameters. (As in Figure 11, we show as blue histograms the number of sample points in each interval). In Figure 12a, it is seen that MDI is strongly correlated with the binned V values; the linear correlation coefficient is $r = 0.88$. In contrast, there is a negative correlation ($r = -0.37$) for mean MDI versus δB (ENLIL) (Figure 12b). The correlation of mean MDI with hybrid VB_s is strong in absolute value (Figure 12c), and the correlation is positive ($r = 0.56$) for the binned data, although the high correlation in this case is in part the result of a few extreme values of VB_s; the vast majority of values of MDI lie in the VB_s range of 1–10 mV/m. The results presented in Figure 12 nonetheless indicate that the hybrid index VB_s and the high-frequency magnetospheric activity index are correlated, as would be expected for strong interplanetary electric field forcing of magnetospheric fluctuations.

[35] As a further illustration of the use of ENLIL-derived solar wind and IMF parameters, we show energetic particle burst data [*Ho et al*., 2011, 2012] in Figure 13. Rather than use the EPS events analyzed in detail by *Ho et al*. [2012], we use the simpler and more robust energetic electron burst data set (energy $E \geq 20$ keV) detected by MESSENGER's Neutron Spectrometer (NS) [see *Ho et al*., 2011]. As seen in Figure 13, there is wide scatter in the peak NS counting rates (counts/s) when plotted versus V (ENLIL). The linear correlation coefficient between the logarithm of the individual NS count rate values and V is only $r = 0.34$. However, examination of mean values (solid black histogram) or median values (dashed red histogram) indicates an obvious positive relationship between the NS electron bursts and the solar wind speed forcing. Note that the blue line in Figure 13 is the least squares fit to individual points; the trend line agrees well with the histogram of mean and median values.

[36] A comparison of NS count rates versus the ENLIL-derived solar wind temperature is shown in Figure 14. We compute that the logarithm of the NS count rate versus the mean value of T has a correlation coefficient $r = 0.930$. However, as with the comparison with V, the individual NS samples show a much more considerable scatter ($r = 0.25$). Despite this scatter, these comparisons show that energetic particle bursts are generally modulated by solar wind forcing, even though internal magnetospheric processes and properties must be playing key roles as well.

[37] As a last example, we explore the utility of ENLIL results for ordering and organizing measurements of Mercury's exosphere made with the Mercury Atmospheric and Surface Composition Spectrometer (MASCS) [*McClintock and Lankton*, 2007] on the MESSENGER spacecraft. Recent MASCS observations of the density of neutral sodium on Mercury's equatorial dayside [e.g., *Cassidy et al*., 2012] have shown strong seasonal changes.

[38] In Figure 15 we show what we call the dayside sodium (Na) "exospheric index" (EI). This index is the zenith column density inferred by MASCS [*Cassidy et al*., 2012] times the photoionization rate for Na, which yields the column-integrated Na ion production rate. Figure 15a shows EI versus ENLIL-derived solar wind temperature (T). Also shown in Figure 15a are histograms of mean and median values. The scattered points have almost no correlation ($r = -0.06$) with T. The red line is the least squares fit of EI versus the binned T and the correlation coefficient is $r = 0.55$. Figure 15b shows the EI values versus ENLIL-derived solar wind density (n). As is evident, the EI values versus binned n value show a much stronger negative correlation ($r = -0.95$).

[39] Although the results in Figure 15b may suggest a substantial control of dayside exospheric Na production by solar wind parameters (especially n), we note that *Cassidy et al*. [2012] found a strong dependence of low-altitude Na on Mercury orbital true anomaly. As depicted in Figure 4, solar wind density and other solar wind quantities are strongly dependent on Mercury season (i.e., the planet's radial distance from the Sun), so we infer that the relationships in Figure 15b are controlled by Mercury's distance from the Sun. Measurements of Na at higher latitudes and high altitudes, as well as measurements of other exospheric species, might clarify the dependence of exospheric properties on variations in solar wind conditions. In Figure 15c, we show the EI values plotted versus the detrended density values (δn) from Figure 7. We see that there is a weaker dependence of EI on the binned δn values ($r = -0.66$).

[40] A compilation of the correlation coefficients associated with each of the regression fits performed in this study is given in Table 1. Essentially all of the fits were first performed between the WSA-ENLIL model parameters and the primary data-derived values or indices. These (generally) low correlation coefficients are shown in the parenthetical values in Table 1. We also show the (generally) higher correlation coefficients between the ENLIL parameters and the binned parameters in the figures above. Obviously, binning or smoothing of data greatly (and artificially) increases the correlation strength.

5. Discussion and Conclusions

[41] In this paper we have shown several comparisons between a widely used space weather modeling tool (WSA-ENLIL) and direct measurements of solar wind and IMF properties near Mercury as measured by instruments on the MESSENGER spacecraft. As noted here, there are well-understood reasons, due to instrument placement and

spacecraft pointing constraints, that the plasma instrument (FIPS) on MESSENGER cannot always sample the solar wind distribution functions adequately [see *Gershman et al*., 2012]. From present as well as prior work [e.g., *Baker et al*., 2009, 2011], we know that the most challenging solar wind measurement to obtain is the complete number density. However, new retrieval methods [*Gershman et al*., 2012] show that quite often it is possible to obtain sound estimates of solar wind speed and temperature. Our comparisons of data and model results in this paper show generally good agreement for those times when FIPS was able to retrieve such information.

[42] The magnetic field data from MESSENGER are generally more complete and "cleaner" than the plasma measurements throughout the orbit of Mercury. We have shown here that the "ambient" WSA-ENLIL model values for the IMF strength (B) agree well with the baseline measurements of the MESSENGER Magnetometer. The major discrepancies between MAG measurements and ENLIL results can be attributed to transient solar wind events associated with CMEs and interplanetary shock waves. We have also suggested that the cone model extension to the ambient WSA-ENLIL code may help us account for the most powerful CME events in the 2011 data analysis interval.

[43] Some of the utility of the WSA-ENLIL results for organizing MESSENGER magnetosphere and exosphere observations has been demonstrated here. We have shown that model outputs such as V and T, as well as composite parameters such as P_{dyn}, provide order to plasma boundary locations. We have also shown that the ENLIL-related indices and solar wind forcing parameters are evidently related to magnetospheric activity levels and energetic particle burst properties.

[44] We draw from our experience and analyses presented here that tools originally intended for Earth-based space weather purposes can have much broader and more general applications. With the use of WSA-ENLIL, we can provide contextual information for planetary studies that simply would not otherwise be available. Such modeling can clearly help fill gaps that exist in the record of in situ spacecraft observations. Also, the evidence from our research suggests that WSA-ENLIL model values can be specified throughout the inner heliosphere and can provide information in support of ground-based planetary observations and campaigns. As a general matter, we believe that the work reported here demonstrates that solar wind modeling tools can beneficially bring heliospheric science expertise to bear on planetary exploration programs.

[45] **Acknowledgments.** The MESSENGER project is supported by the NASA Discovery Program under contracts NASW-00002 to the Carnegie Institution of Washington and NAS5-97271 to The Johns Hopkins University Applied Physics Laboratory. The modeling techniques described here were originally developed under the auspices of the National Science Foundation's Center for Integrated Space Weather Modeling (CISM).

References

Alexeev, I. I., et al. (2010), Mercury's magnetospheric magnetic field after the first two MESSENGER flybys, *Icarus*, *209*, 29–39, doi:10.1016/j.icarus.2010.01.024.

Anderson, B. J., M. H. Acuña, D. A. Lohr, J. Scheifele, A. Raval, H. Korth, and J. A. Slavin (2007), The Magnetometer instrument on MESSENGER, *Space Sci. Rev.*, *131*, 417–450.

Anderson, B. J., M. H. Acuña, H. Korth, M. E. Purucker, C. L. Johnson, J. A. Slavin, S. C. Solomon, and R. L. McNutt Jr. (2008), The structure of Mercury's magnetic field from MESSENGER's first flyby, *Science*, *321*, 82–85.

Anderson, B. J., et al. (2010), The magnetic field of Mercury, *Space Sci. Rev.*, *152*, 307–339.

Anderson, B. J., C. L. Johnson, H. Korth, R. M. Winslow, J. E. Borovsky, M. E. Purucker, J. A. Slavin, S. C. Solomon, M. T. Zuber, and R. L. McNutt Jr. (2012), Low-degree structure in Mercury's planetary magnetic field, *J. Geophys. Res.*, *117*, E00L12, doi:10.1029/2012JE004159.

Andrews, G. B., et al. (2007), The Energetic Particle and Plasma Spectrometer instrument on the MESSENGER spacecraft, *Space Sci. Rev.*, *131*, 523–526.

Arge, C. N., and V. J. Pizzo (2000), Improvement in the prediction of SW conditions using near-real-time solar magnetic field updates, *J. Geophys. Res.*, *105*, 10,465–10,479.

Arge, C. N., J. G. Luhmann, D. Odstrcil, C. J. Schrijver, and Y. Li (2004), Stream structure and coronal sources of the solar wind during the May 12th, 1997 CME, *J. Atmos. Sol. Terr. Phys.*, *66*, 1295–1309.

Baker, D. N., et al. (1996), The neutral line model of substorms: Past results and present view, *J. Geophys. Res.*, *101*, 12,995–13,010.

Baker, D. N., et al. (2009), Space environment of Mercury at the time of the first MESSENGER flyby: Solar wind and interplanetary magnetic field modeling of upstream conditions, *J. Geophys. Res.*, *114*, A10101, doi:10.1029/2009JA014287.

Baker, D. N., et al. (2011), The space environment of Mercury at the times of the second and third MESSENGER flybys, *Planet. Space Sci.*, *59*, 2066–2074, doi:10.1016/j.pss.2011.01.018.

Cassidy, T. A., A. W. Merkel, W. E. McClintock, M. H. Burger, R. M. Killen, M. Sarantos, A. L. Sprague, R. J. Vervack Jr., and S. C. Solomon (2012), Mercury's seasonal sodium exosphere, *EPSC Abstr.*, *7*, EPSE2012-766-1.

Gershman, D. J., T. H. Zurbuchen, L. A. Fisk, J. A. Gilbert, J. R. Raines, B. J. Anderson, C. W. Smith, H. Korth, and S. C. Solomon (2012), Solar wind alpha particles and heavy ions in the inner heliosphere, *J. Geophys. Res.*, *117*, A00M02, doi:10.1029/2012JA017829.

Ho, G. C., et al. (2011), MESSENGER observations of transient bursts of energetic electrons in Mercury's magnetosphere, *Science*, *333*, 1866–1868, doi:10.1126/science.121101.

Ho, G. C., S. M. Krimigis, R. E. Gold, D. N. Baker, B. J. Anderson, H. Korth, J. A. Slavin, R. L. McNutt Jr., and S. C. Solomon (2012), Spatial distribution and spectral characteristics of energetic electrons in Mercury's magnetosphere, *J. Geophys. Res.*, *117*, A00M04, doi:10.1029/2012JA017983.

Johnson, C. L., et al. (2012), MESSENGER observations of Mercury's magnetic field structure, *J. Geophys. Res.*, *117*, E00L14, doi:10.1029/2012JE004217.

Korth, H., B. J. Anderson, T. H. Zurbuchen, J. A. Slavin, S. Perri, S. A. Boardsen, D. N. Baker, S. C. Solomon, and R. L. McNutt Jr. (2011), The interplanetary magnetic field environment at Mercury's orbit, *Planet. Space Sci.*, *59*, 2075–2085.

McClintock, W. E., and M. R. Lankton (2007), The Mercury Atmospheric and Surface Composition Spectrometer for the MESSENGER mission, *Space Sci. Rev.*, *131*, 481–521.

McPherron, R. L., C. T. Russell, and M. Aubry (1973), Satellite studies of magnetospheric substorms on August 15, 1978, 9, phenomenological model for substorms, *J. Geophys. Res.*, *78*, 3131–3149.

Odstrcil, D., and V. J. Pizzo (1999), Three-dimensional propagation of coronal mass ejections (CMEs) in a structured solar wind flow 1. CME launched within the streamer, *J. Geophys. Res.*, *104*, 483–492.

Odstrcil, D., V. J. Pizzo, J. A. Linker, P. Riley, R. Lionello, and Z. Mikic (2004a), Initial coupling of coronal and heliospheric numerical magnetohydrodynamic codes, *J. Atmos. Sol. Terr. Phys.*, *66*, 1311–1326, doi:10.1016/j.jastp.2004a.04.007.

Odstrcil, D., P. Riley, and X. P. Zhao (2004b), Numerical simulation of the 12 May 1997 interplanetary CME event, *J. Geophys. Res.*, *109*, A02116, doi:10.1029/2003JA010135.

Pizzo, V., G. Millward, A. Parsons, D. Biesecker, S. Hill, and D. Odstrcil (2011), Wang-Sheeley-Arge-ENLIL cone model transitions to operations, *Space Weather*, *9*, S033004, doi:10.1029/ 2011SW000663.

Schatten K. H., J. M. Wilcox, and N. F. Ness (1969), A model of interplanetary and coronal magnetic fields, *Sol. Phys.*, *6*, 442–455, doi:10.1007/BF00146478.

Shue, J.-H., J. K. Chao, H. C. Fu, C. T. Russell, P. Song, K. K. Khurana, and H. J. Singer (1997), A new functional form to study the solar wind control of the magnetopause size and shape, *J. Geophys. Res.*, *102*, 9497–9511.

Siscoe, G. L., N. F. Ness, and C. M. Yeates (1975), Substorms on Mercury?, *J. Geophys. Res.*, *80*, 4359–4363.

Slavin, J. A., et al. (2009), MESSENGER observations of magnetic reconnection in Mercury's magnetosphere, *Science*, *324*, 606–610.

Slavin, J. A., et al. (2010), MESSENGER observations of extreme loading and unloading of Mercury's magnetic tail, *Science*, *329*, 665–668, doi:10.1126/science.1188067.

Sundberg, T., et al. (2012), MESSENGER observations of dipolarization events in Mercury's magnetotail, *J. Geophys. Res.*, *117*, A00M03, doi:10.1029/2012JA017756.

Wang, Y.-M., and N. R. Sheeley Jr. (1992), On potential field models of the solar corona, *Astrophys. J.*, *392*, 310–319.

Winslow, R. M., C. L. Johnson, B. J. Anderson, H. Korth, J. A. Slavin, M. E. Purucker, and S. C. Solomon (2012), Observations of Mercury's northern cusp region with MESSENGER's Magnetometer, *Geophys. Res. Lett.*, *39*, L08112, doi:10.1029/2012GL051472.

Xie, H., L. Ofman, and G. Lawrence (2004), Cone model for halo CMEs: Applications to space weather forecasting, *J. Geophys. Res.*, *109*, A03109, doi:10.1029/2003JA010226.

Zhao, X. P., S. P. Plunkett, and W. Liu (2002), Determination of geometrical and kinematical properties of halo coronal mass ejections using the cone model, *J. Geophys. Res.*, *107*, 1223, doi:10.1029/2001JA009143.

Zurbuchen, T. H., G. Gloeckler, J. C. Cain, S. E. Lasley, and W. Shanks (1998), A low-weight plasma instrument to be used in the inner heliosphere, in Conference on Missions to the Sun II, edited by C. M. Korendyke, Proceedings of the Society of Photo-Optical Instrumentation Engineers, vol. 3442, pp. 217–224, Bellingham, Wash.